Spin transport parameters of NbN thin films characterized by spin pumping experiments

K. Rogdakis,[1,*] A. Sud,[1] M. Amado,[2] C. M. Lee,[2] L. McKenzie-Sell,[2] K. R. Jeon,[2] M. Cubukcu,[1] M. G. Blamire,[2] J. W. A. Robinson,[2] L. F. Cohen,[3] and H. Kurebayashi[1,†]

[1]*London Centre for Nanotechnology, University College London, London WC1H 0AH, England, United Kingdom*
[2]*Department of Materials Science and Metallurgy, University of Cambridge, Cambridge CB3 0FS, England, United Kingdom*
[3]*The Blackett Laboratory, Imperial College London, London SW7 2AZ, England, United Kingdom*

(Received 4 September 2018; revised manuscript received 14 November 2018; published 14 January 2019)

We present measurements of ferromagnetic resonance driven spin pumping and inverse spin Hall effect in NbN/$Y_3Fe_5O_{12}$ (YIG) bilayers. A clear enhancement of the (effective) Gilbert damping constant of the thin-film YIG was observed due to the presence of the NbN spin sink. By varying the NbN thickness and employing spin-diffusion theory, we have estimated the room-temperature values of the spin-diffusion length and the spin Hall angle in NbN to be 14 nm and -1.1×10^{-2}, respectively. Furthermore, we have determined the spin mixing conductance of the NbN/YIG interface to be $10\,\mathrm{nm}^{-2}$. The experimental quantification of these spin transport parameters is an important step towards the development of superconducting spintronic devices involving NbN thin films.

DOI: 10.1103/PhysRevMaterials.3.014406

I. INTRODUCTION

The extraction of key functional materials parameters associated with electron transport is important for the development of new solid-state device schemes as well as testing prototypes. In the field of spintronics, the spin Hall angle (θ_{SH}) represents the strength of spin Hall effect (SHE) [1] that converts charge currents into spin currents via the relativistic spin-orbit interaction. The spin-diffusion length (l_{SD}) [2] is a parameter that describes the distance over which nonequilibrium spin currents can diffuse before dissipation and is crucial in determining the useful device dimensions of future spintronic applications. Moreover, the spin angular momentum transfer across a ferromagnetic (FM) and nonmagnetic (NM) interface can be parametrized by the spin mixing conductance ($g_r^{\uparrow\downarrow}$), which governs the spin current generation efficiency in spin pumping processes [3]. These spin transport parameters can be determined by employing different measurement techniques. For example, it is possible to use lateral spin valves to quantify l_{SD} and θ_{SH} in nonmagnetic materials [4–7]. Spin pumping [3,8,9] is another established method to investigate spin transport parameters in a variety of materials, such as metals [10], inorganic [11,12] and organic semiconductors [13,14], graphene [15], and topological insulators [16]. It should be noted that spin pumping relies on the transfer of angular momentum from a ferromagnet with precessing moments into an adjacent nonmagnetic layer and does not suffer from the conductance mismatch problem, which causes difficulties in electrical spin injection through ohmic contacts [11]. Using a FM conductor as spin injector in a spin pumping experiment can potentially give rise to microwave (MW) induced photovoltages [17] due to time-varying resistance changes produced by the magnetic precession coupled with a time-varying current, as well as the inverse spin Hall effect (ISHE) in the FM layers [18,19]. The use of FM insulators such as $Y_3Fe_5O_{12}$ (YIG) to conduct spin pumping experiments has the advantage because these effects are negated. In addition, YIG has a low bulk Gilbert damping constant ($\alpha \simeq 6.7 \times 10^{-5}$) and a high Curie temperature ($T_C = 560\,\mathrm{K}$), enabling efficient spin pumping at room temperature (RT) [20].

In this paper, we report spin pumping in thin-film YIG/NbN bilayers with the aim of extracting multiple spin transport parameters of NbN thin films in the normal state. NbN is a key material for superconducting (SC) spintronics [21] with a bulk T_C of approximately 16.5 K, a SC energy gap of 2.5 meV, and a SC coherence length of 5 nm [22]. NbN is increasingly used in the field of SC spintronics, for example in spin-filter Josephson junctions [23–25] and to demonstrate spectroscopic evidence for odd frequency (spin-triplet) superconductivity at the interface with GdN [26]. Recently, Wakamura *et al.* observed an unprecedented enhancement of the SHE at 2 K, interpreted in terms of quasiparticle mediated transport [27]. Quasiparticle spin transport has also been investigated by spin pumping and by monitoring the spin Seebeck effect [28,29]. To the best of our knowledge, spin transport parameters in NbN such as l_{SD} and θ_{SH} have only been extracted by Wakamura *et al.* [27] by the spin absorption method in lateral spin valves, and it is vitally important to extract these parameters also by other characterization techniques and with NbN grown by different growth methods. This can, for example, help us to understand whether spin transport parameters in NbN have a significant dependence on the growth conditions. In our paper, by using high-quality epitaxial thin-film YIG it is possible to observe a modulation of the Gilbert damping constant (α) with NbN thickness and therefore extract l_{SD} of NbN (14 nm) and $g_r^{\uparrow\downarrow}$ of the YIG/NbN interface ($10\,\mathrm{nm}^{-2}$). Furthermore, we have investigated the NbN thickness

*rogdakis7@gmail.com
†h.kurebayashi@ucl.ac.uk

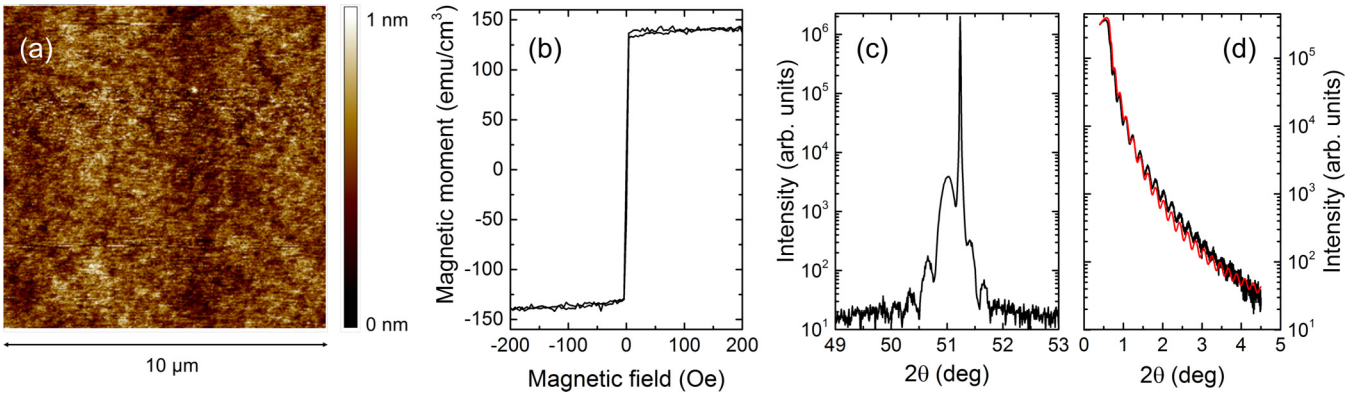

FIG. 1. Structural and magnetic properties of a bare (111)-oriented YIG film (nominally 60 nm thick) used in this paper and deposited onto GGG. (a) 10×10 μm AFM topography scan showing a root-mean-square roughness of less than 0.16 nm. (b) Magnetization hysteresis loops characterized by a superconducting quantum interference device magnetometer showing a saturation volume magnetization of 140 ± 3 emu cm^{-3}. (c) High angle x-ray-diffraction data demonstrating (111) orientation with visible Laue fringes on the (444) and (888) diffraction peaks characteristic of layer-by-layer growth. (d) Low angle x-ray reflectometry data (black) with a best-fit (red) curve from which we estimate a nominal thickness of 60 ± 2 nm.

dependence of the ISHE voltage (V_{ISHE}) and have determined θ_{SH} of NbN (-1.1×10^{-2}) by the spin pumping technique. We compare l_{SD} extracted by three independent methods, namely, the thickness dependence of α and V_{ISHE} as well as Hanle spin precession, and we find good agreement between them. Determining the normal-state spin transport parameters in NbN from spin pumping induced ISHE is important and enables the comparison between parameters extracted using various techniques from different research groups [e.g., [27–29]]. By accumulation of a body of results, we will then be able to understand the fundamental nature of SHE and spin transport in NbN, which can be useful and transferable to future spintronics research using SC NbN [21,30].

II. MATERIAL GROWTH

Epitaxial YIG thin films are grown on (111)-oriented GGG single-crystal substrates by pulse laser deposition (PLD) in a UHV chamber with a base pressure better than 5×10^{-7} mbar. Prior to film growth, the GGG substrate is ultrasonically cleaned by acetone and isopropyl alcohol and annealed *ex situ* at 1000 °C in a constant O_2 flow environment for 8 h. The YIG is deposited from a stoichiometric (polycrystalline) target using a KrF excimer laser (248-nm wavelength), with a nominal energy of 450 mJ and fluence of 2.2 W cm^{-2} in 0.12 mbar of O_2 at 680 °C, and pulse frequency of 4 Hz for 60 min. The YIG is postannealed at 750 °C for 1.5 h in 0.5 mbar partial pressure of static O_2 and subsequently cooled to RT at a rate of -10 K/ min. Atomic force microscopy (AFM) reveals that a root-mean-squared roughness of the YIG films is less than 0.16 nm over 10×10-μm scan size [Fig. 1(a)]. The YIG films were characterized by a SC quantum interference device (SQUID) magnetometer and have a saturation magnetization (M_{S}) of 140 ± 3 emu cm^{-3} [Fig. 1(b)], which matches the bulk value [31]. In Fig. 1(c) we have plotted a high angle x-ray-diffraction trace of the same film where Laue fringes indicate layer-by-layer growth of YIG and good lattice matching with the substrate. Figure 1(d) shows low-angle x-ray reflectivity from a YIG film, and from the decay and angle separation of the Kiessig fringes we determined a nominal thickness $t_{\mathrm{YIG}} = 60 \pm 2$ nm. Following the growth of YIG, films were directly transferred in air to a UHV sputter deposition system with a base pressure of 1×10^{-9} mbar. NbN is grown by reactive sputtering in a gas mixture of argon (72%) and nitrogen (28%) with the deposition rate of 85 nm min^{-1}. The growth temperature is RT, giving polycrystalline NbN layers. We grew NbN with different thicknesses (t_{NbN}) from 5 to 50 nm.

A. Ferromagnetic resonance setup and spin pumping measurements

Ferromagnetic resonance (FMR) is performed using a broadband coplanar waveguide (CPW) and ac-field modulation technique as illustrated in Fig. 2(a). The samples are placed face down on top of the CPWs where an insulator tape is used for electrical insulation. We generate dc (H) and ac (h_{ac}) magnetic fields by electromagnets and the absorbed power at the modulation frequency is measured by a MW power detector and a lock-in amplifier while H is swept. An input MW power (P_{MW}) of 100 mW is used unless otherwise stated. We kept the modulation field amplitude (h_{ac}) smaller than the measured FMR linewidths of all samples tested, in order to avoid artifacts by strong modulation. The magnetic field is applied along different in-plane and out-of-plane directions related to the samples as shown in Fig. 2(a). The FMR absorption (V_P) was measured using a MW power detector for different frequencies typically ranging from 2 to 12 GHz as depicted in Fig. 2(b) (for a sample with $t_{\mathrm{NbN}} = 10$ nm). For each scan, the resonance field (H_{res}) and the half width at half maximum linewidth (ΔH) of the FMR signal are determined by a fit using differential forms of symmetric and antisymmetric Lorentzian functions (Appendix A). Figure 2(c) shows the frequency dependence of the extracted H_{res} for different NbN thicknesses. The curves of the frequency dependence for all samples, including $t_{\mathrm{NbN}} = 0$ nm, overlap, suggesting no significant modification of the YIG magnetic anisotropy due to the presence of NbN. We note here that the effective magnetization (M_{eff}) extracted from the fits for each sample shows larger values than the M_s

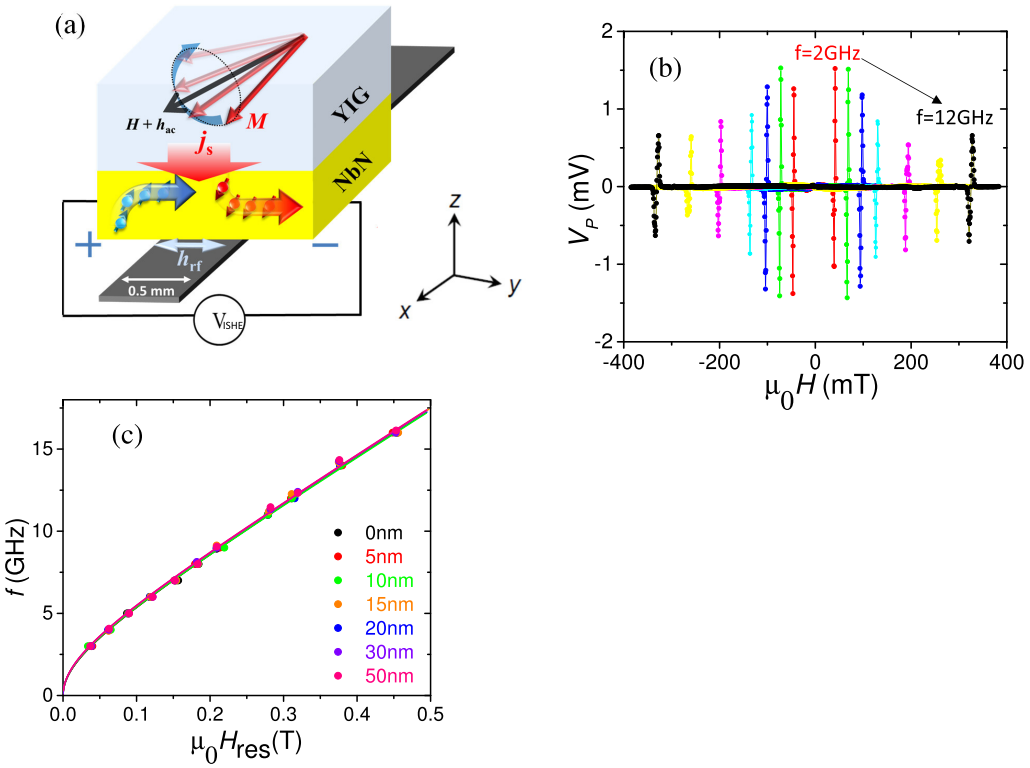

FIG. 2. (a) A schematic of the spin pumping setup. The lateral area of all samples is $5 \times 5\,\mathrm{mm}^2$. MW magnetic fields ($h_{\mathrm{rf}}$) were generated by the transmission line to generate magnetic dynamics in the YIG film. Spin currents (j_s) were emitted at the YIG/NbN interface, which can induce ISHE voltages detected through the two electrodes attached to the edges of the sample. We simultaneously measured the FMR absorption signal as a voltage in a microwave power meter (V_{P}) connected to the microwave line and the ISHE signal (V_{ISHE}). (b) FMR absorption measurements for different MW frequencies. (b) FMR absorption measurements for different MW frequencies. Voltages in our MW power detector were measured while magnetic fields were swept. Dots in red, green, blue, cyan, pink, yellow, and black represent measurement results for 3, 4, 5, 6, 8, 10, and 12 GHz, respectively. (c) A plot of frequency vs FMR field (H_{res}) for samples with different NbN thicknesses. Dots represent experimental results and curves are produced by fitting using the Kittel formula.

value measured in the SQUID. This enhanced M_{eff} has often been observed in other thin-film studies [32,33] and a detailed understanding of this lies outside of the scope of the present paper. For spin transport analysis discussed later, we use the values extracted by SQUID measurements since they are more direct measurements of magnetization, while we confirmed that the discrepancy between M_s and M_{eff} does not alter the calculated spin transport parameters significantly. Although the magnetic anisotropies of the YIG films are unchanged with or without the presence of NbN, the magnetization relaxation

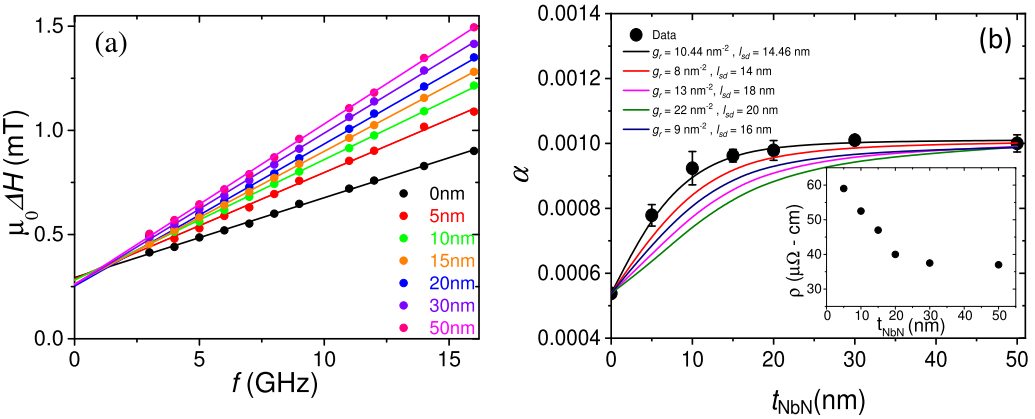

FIG. 3. (a) Frequency dependence of FMR linewidth of YIG/NbN samples with different NbN thicknesses. Experimental data (filled points) is fitted by a linear line $\Delta H = \Delta H_0 + (4\pi\alpha/\gamma) f$, where ΔH_0 and γ describe the inhomogeneous broadening and the gyromagnetic ratio respectively, from which the Gilbert damping coefficient α is extracted. (b) Plots of α for different YIG/NbN samples. Equation (1) was used to fit to the thickness dependence with the spin-diffusion length and the real part of mixing conductance as fitting parameters. The inset depicts the resistivity as a function of NbN thickness.

of YIG represented by ΔH shows a clear dependence on t_{NbN} as shown in Fig. 3(a). With a linear fit to the data for each thickness using $\Delta H = \Delta H_0 + (4\pi\alpha/\gamma)f$ where ΔH_0 and γ describe the inhomogeneous broadening and the gyromagnetic ratio, respectively, we have quantified α for each sample as shown in Fig. 3(b). $\alpha = (5.4 \pm 0.2) \times 10^{-4}$ was obtained for bare YIG, which compares well to previously reported values [34,35]. A gradual increase of α is observed with increasing NbN thickness, in agreement with spin pumping through the YIG/NbN interface where the α dependence with t_{NbN} is given by [36]

$$\alpha(t_{\mathrm{NbN}}) = \alpha_0 + \left(\frac{g_L \mu_B g_r^{\uparrow\downarrow}}{4\pi M_s t_{\mathrm{YIG}}}\right)\left[1 + \frac{g_r^{\uparrow\downarrow}\rho_{\mathrm{NbN}} l_{\mathrm{SD}} e^2}{2\pi\hbar \tanh\left(\frac{t_{\mathrm{NbN}}}{l_{\mathrm{SD}}}\right)}\right]^{-1}. \quad (1)$$

Here, α_0 is the Gilbert damping constant for $t_{\mathrm{NbN}} = 0$ nm and the second term represents the damping enhancement by spin pumping into NbN, g_L is the free-electron Landé factor which is assumed equal to 2; $g_r^{\uparrow\downarrow}$ is the effective real-part spin mixing conductance across the NbN/YIG interface; ρ_{NbN} is the resistivity of NbN which was measured for each sample [see inset of Fig. 3(b)]; and e is the electron charge. A best fit of the data in Fig. 3(b) using Eq. (1) yields $g_r^{\uparrow\downarrow} = 10 \pm 2\,\mathrm{nm}^{-2}$ and $l_{\mathrm{SD}} = 14 \pm 3$ nm. The extracted l_{SD} can be well compared with the value (7 nm) by Wakamura *et al.* [27] using the spin absorption method in lateral spin valve devices. We also found that the spin coupling of NbN/YIG is as good as heavy-metals/YIG interfaces since $g_r^{\uparrow\downarrow}$ is comparable to those of YIG/Pt, YIG/Ta, and YIG/W [35]. We note from analytic calculations (Appendix B) that the additional damping expected from eddy currents cannot explain the observed NbN thickness dependence of α.

We now discuss the ISHE voltage (V_{ISHE}) measurements. In Figs. 4(a) and 4(b) we show typical data sets for V_{ISHE} (for direct comparison we present also corresponding V_p data) for $t_{\mathrm{NbN}} = 20$ nm and $f = 3$ GHz. Note that, since we used

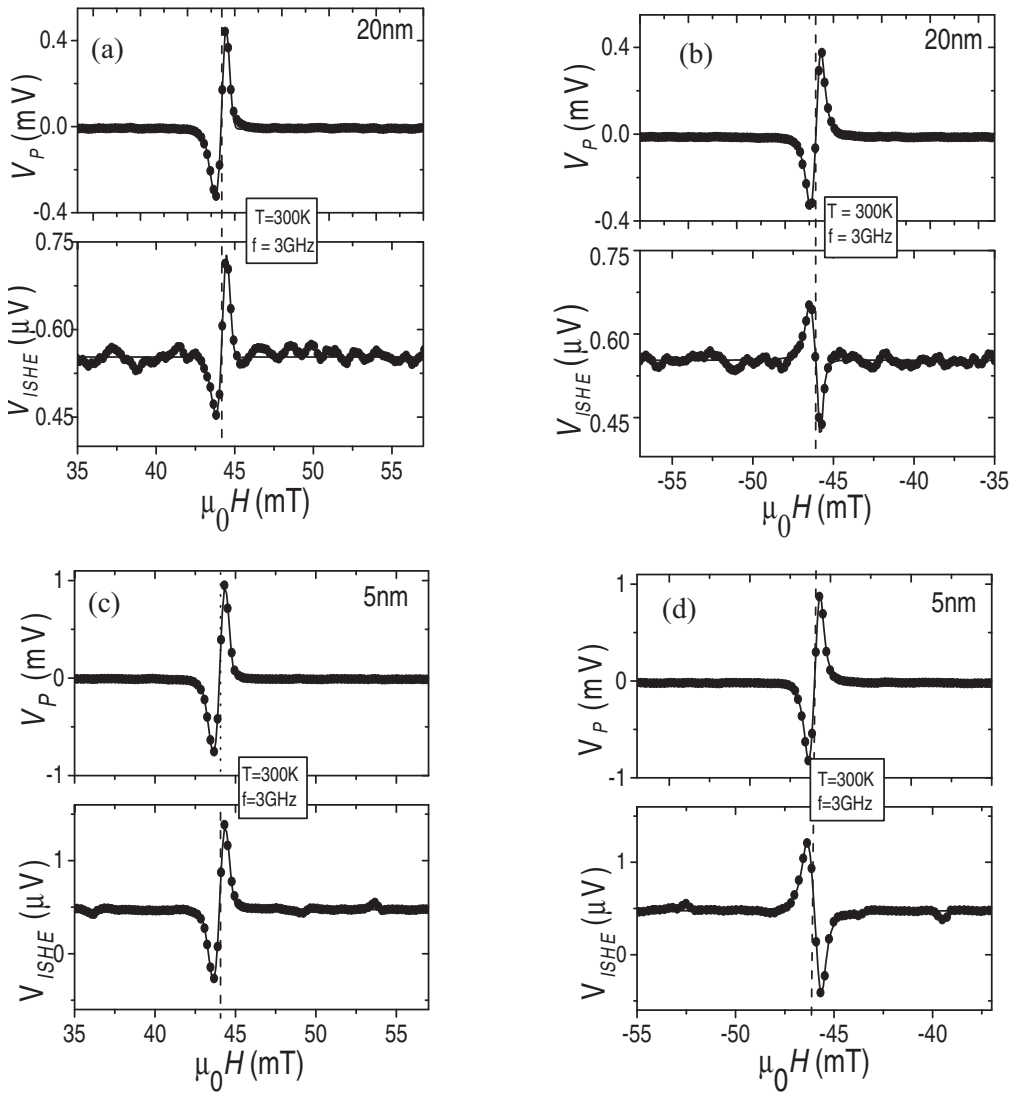

FIG. 4. ISHE measurements. Simultaneous measurements of FMR absorption and ISHE voltages for positive (a) and negative (b) magnetic field values for a $t_{\mathrm{NBN}} = 20$ nm sample. Corresponding data for $t_{\mathrm{NBN}} = 5$ nm are depicted in (c) and (d), respectively. Both V_{P} and V_{ISHE} peaks appear at the same magnetic field, confirming that the voltages were generated when YIG magnetic moments were precessing. The sign change in voltage peaks observed between the positive and negative magnetic field regions is consistent with the spin pumping/ISHE picture.

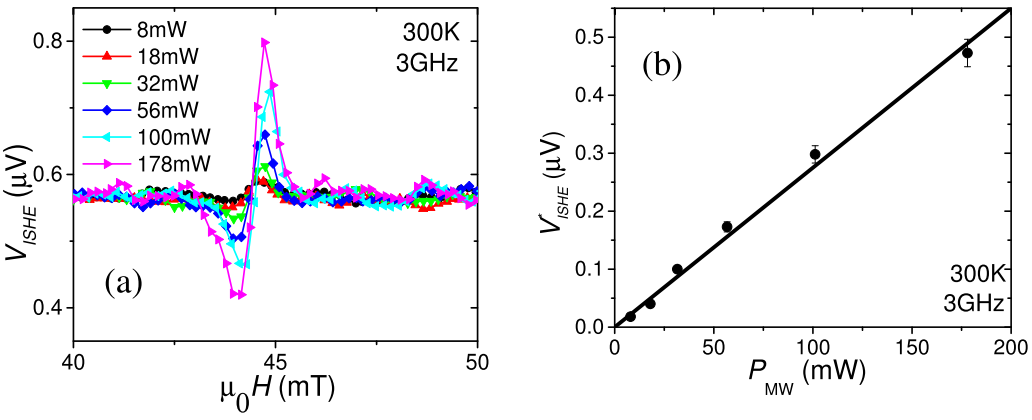

FIG. 5. Microwave power dependent measurements. (a) ISHE voltage measurements with different insertion powers (P_{MW}). (b) A plot of ISHE voltage peak to peak amplitude (V^*_{ISHE}) as a function of P_{MW}. V_{ISHE} scales with P_{MW} as expected from the spin pumping theory in the linear regime.

the lock-in ac field modulation method for both detections, the curves represent the derivative of the signals without the ac field modulation: for both V_p and V_{ISHE} a symmetric Lorentzian line shape is expected without the ac field modulation. As expected from spin pumping and ISHE, we observe a clear V_{ISHE} peak at the YIG precession frequency. By changing the sign of H [observe the sign of magnetic field axis for Figs. 4(a) and 4(b)], we observe a sign change of V_{ISHE} in agreement with the symmetry of spin pumping [37]. Corresponding measurements for $t_{\mathrm{NbN}} = 5$ nm are depicted in Figs. 4(c) and 4(d). By using the known ac field modulation amplitude as well as differential forms of symmetric and antisymmetric Lorentzian functions (Appendix A), we quantify the peak amplitude of ISHE voltage defined as V^*_{ISHE}. The P_{MW} dependence of V^*_{ISHE} shown in Figs. 5(a) and 5(b) suggests that V^*_{ISHE} is proportional to P_{MW}, consistent with standard spin pumping theory [36].

We have also performed H angular dependent measurements of V^*_{ISHE} along in-plane and out-of-plane directions of the NbN/YIG films. The in-plane angular dependence of the spin pumping experiment follows the expression $V^*_{\mathrm{ISHE}} \propto \boldsymbol{\epsilon_x} \cdot (\boldsymbol{J_s} \times \boldsymbol{\sigma}) \cdot |\boldsymbol{\sigma} \times \boldsymbol{h_{rf}}|$ where the first part is due to the ISHE symmetry, $E_{\mathrm{ISHE}} \propto (\boldsymbol{J_s} \times \boldsymbol{\sigma})$, multiplied by the amplitude of magnetic torque generated by MW-induced magnetic field $|\boldsymbol{\sigma} \times \boldsymbol{h_{rf}}|$; here, $\boldsymbol{\epsilon_x}$ is the unit vector along the x direction in the measurement's framework shown in Fig. 2(a). The first component gives a $\cos\theta$ dependence whereas the second produces a $|\cos\theta|$ dependence, which combined nicely matches our experimental results shown in Fig. 6(a). The rationale to plot $V^*_{\mathrm{ISHE}} t_{\mathrm{NbN}}/\rho_{\mathrm{NbN}}$ against t_{NbN} is to include the thickness dependence of ρ_{NbN}, allowing us to fit the data points based on bare NbN as well as those of the YIG/NbN bilayers. In addition, this analysis can display the asymptotic behavior of the data and fit curves towards the long thickness limit. The in-plane symmetry reconfirms that spin rectification effects are not a dominant mechanism in our measurements since in this case a higher-order sin 2θ component is expected in the voltage symmetry [17]. We also measured the out-of-plane angular dependence of V^*_{ISHE} as shown in Fig. 6(b) and moreover we applied the Hanle precession model [38] to fit our data. In this case the out-of-plane V^*_{ISHE} is given by

$$V^*_{\mathrm{ISHE}}(\phi) \propto \left\{ \cos(\phi)\cos(\phi - \phi_M) + \sin\phi \sin(\phi - \phi_M) \times \left[\frac{1}{1 + (\omega_L \cdot \tau_s)^2} \right] \right\} \tag{2}$$

where $\omega_L = g_L \mu_B (\mu_0 H)/\hbar$ is the Larmor frequency, and τ_s is the spin-relaxation time in NbN; ϕ and ϕ_M represent the angle between the z axis and H and the equilibrium magnetic

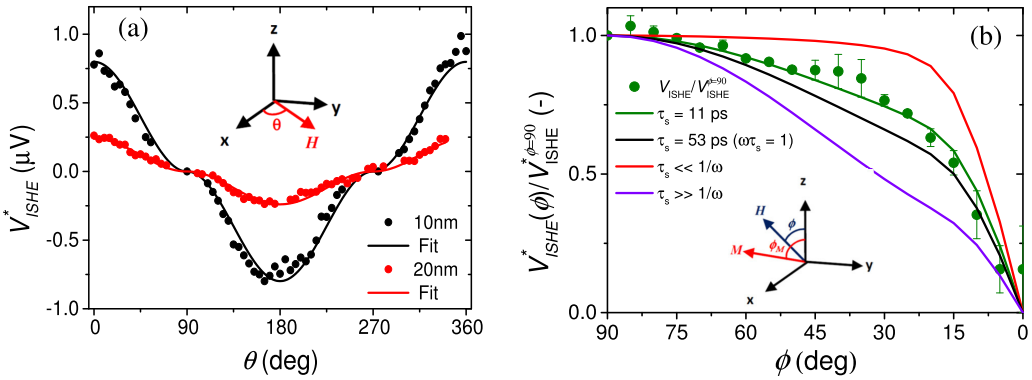

FIG. 6. In-plane (a) and out-of-plane (b) angular dependences of V_{ISHE} signal peak to peak amplitude (V^*_{ISHE}). Fit curves in both angular dependences are discussed in the main text. We show fit curves with four different spin-relaxation times (τ_s) in (b) to illustrate how the model curve changes with τ_s. The best-fit curve was produced with $\tau_s = 11 \pm 2$ ps. We define three angles (ϕ, ϕ_M, θ) as depicted in the insets.

moment direction, respectively. By minimizing the total magnetic energy of the FM layer consisting of the Zeeman and demagnetization energy, the following equation is derived to determine the value of ϕ_M with respect to ϕ: $\phi_M = \phi - \arctan[\mathrm{sgn}(\phi)\sqrt{(\frac{\cos(2\phi)+(\frac{\mu_0 H_{\mathrm{res}}}{\mu_0 M_{\mathrm{eff}}})}{\sin(2\phi)})^2 + 1} - (\frac{\cos(2\phi)+(\frac{\mu_0 H_{\mathrm{res}}}{\mu_0 M_{\mathrm{eff}}})}{\sin(2\phi)})]$ [39]. After spin currents are injected inside NbN, they start precessing due to the externally applied H. This is described by the well-known Hanle precession model which is the basis of Eq. (2). The equilibrium spin orientation depends on the precession rate (ω_L) and the spin-relaxation rate ($1/\tau_s$), both of which contribute in the equation. When τ_s is much shorter than $1/\omega_L$, the injected spins do not precess and instead generate V_{ISHE} with spin orientation along M (ϕ_M). This is the case for the red curve in Fig. 6(b). In the opposite extreme condition [depicted as a blue curve in Fig. 6(b)], spins precess many times and dephase along the H orientation (ϕ), resulting in an approximately $\cos(\phi)$ angle dependence. Fitting the data in Fig. 6(b) using Eq. (2) allows us to estimate τ_s. In particular, the best fit of the measured $V^*_{\mathrm{ISHE}}(\phi)$ was obtained, giving an extracted $\tau_s = 11 \pm 2$ ps. This value quantified by the Hanle model can be compared with τ_s independently calculated from the spin-diffusion model as already discussed above, i.e., $\tau_s = (l_{\mathrm{SD}})^2/D$ where D is the Einstein diffusion coefficient (its value equal to $0.4 - 0.56\,\mathrm{cm}^2/\mathrm{s}$ was taken from [40]). Following this approach and by using $l_{\mathrm{SD}} = 14$ nm as extracted from the thickness dependence of damping modulation, we calculated $\tau_s = 3.6$–5.9 ps, which is a fair agreement between the two different τ_s extraction methods.

In the following section, the θ_{SH} of NbN is determined from the thickness dependence of V^*_{ISHE} as shown in Fig. 7. Using the spin transport parameters discussed above and Eq. (3), we estimate the spin current emitted at the NbN/YIG interface, j_s, as well as the value of θ_{SH} extracted by fitting the thickness dependence of V^*_{ISHE} [39]:

$$V^*_{\mathrm{ISHE}} = \left(\frac{w_y \rho_{\mathrm{NbN}}}{t_{\mathrm{NbN}}}\right)\theta_{\mathrm{SH}} l_{\mathrm{SD}} \tanh\left(\frac{t_{\mathrm{NbN}}}{2l_{\mathrm{SD}}}\right) j_s$$

$$\text{where } j_s = \left(\frac{G_r^{\uparrow\downarrow}\hbar}{8\pi}\right)\left(\frac{\mu_0 h_{rf}\gamma}{\alpha}\right)^2 \times \left[\frac{\mu_0 M_s\gamma + \sqrt{(\mu_0 M_s\gamma)^2 + 16(\pi f)^2}}{(\mu_0 M_s\gamma)^2 + 16(\pi f)^2}\right]\left(\frac{2e}{\hbar}\right)$$

$$\text{with } G_r^{\uparrow\downarrow} \equiv g_r^{\uparrow\downarrow}\left[1 + \frac{g_r^{\uparrow\downarrow}\rho_{\mathrm{NbN}} l_{\mathrm{SD}} e^2}{2\pi\hbar\,\tanh\left(\frac{t_{\mathrm{NbN}}}{l_{\mathrm{SD}}}\right)}\right]^{-1}. \quad (3)$$

Here we assume that YIG is a perfect insulator; $\mu_0 h_{rf}$ is the amplitude of MW magnetic field (56 μT for 100 mW); w_y is defined by the width of the MW transmission line. For the data fitting procedure we use θ_{SH} and l_{SD} as free parameters, where the best fitting was achieved for 1.1×10^{-2} and 14 nm, respectively. We also confirmed the sign of θ_{SH} to be negative by comparing YIG/NbN data with a YIG/Pt control sample where Pt is known to have a positive θ_{SH} [1]. We emphasize that the value of l_{SD} extracted by the thickness dependence of V^*_{ISHE} agrees very well with the one extracted from the thickness dependence of damping. The former approach includes spin-orbit and spin transport properties of NbN, whereas the latter is purely related with magnetic properties of YIG. We found that the value we extract by our spin pumping experiments is similar to θ_{SH} quantified by Wakamura *et al.* using lateral spin valve samples ($\theta_{\mathrm{SH}} \sim -1 \times 10^{-2}$) [27] for the temperature region between 20 and 200 K. Although there is difference in temperature between experiments by Wakamura *et al.* and ours, an agreement of the same sign and magnitude in θ_{SH} quantified by different techniques (i.e., spin pumping and spin absorption) has been observed. The value of θ_{SH} of the same material but grown and measured by different research groups can vary rather significantly, for example as in the cases of Pt [41] and some topological insulators [42–44]. Such differences might result from variation in sample quality where the density of scattering impurities can particularly influence θ_{SH} via the extrinsic spin Hall mechanisms [1]. We note that the resistivity of NbN used in the Wakamura *et al.* [27] study measured at 20 K (220 $\mu\Omega$ cm) is roughly three times greater than our NbN films at the same temperature (65 $\mu\Omega$ cm). This highlights that the resistivity and mobility of NbN might be highly growth dependent, possibly due to the stoichiometry of Nb and N as well as the nitrogen vacancy concentration. The NbN spin Hall resistivity of Wakamura *et al.* is 2.2 $\mu\Omega$ cm at 20 K, whereas our spin Hall resistivity at RT is calculated to be 0.5 $\mu\Omega$ cm, which is smaller owing to the resistivity difference. For the relevance of SC spintronics, we also compare our θ_{SH} value with those of Nb thin films reported in previous works. Morota *et al.* measured θ_{SH} of several 4*d* and 5*d* transition metals by the spin absorption method in the lateral spin valve structures [6] including Nb. They quantified θ_{SH} of Nb to be -8.7×10^{-3} at 10 K, which is close to our θ_{SH} in NbN at RT. There is recent work by Jeon *et al.*, who measured $\theta_{\mathrm{SH}} = -1 \times 10^{-3}$ in Nb at RT [39]. Direct comparison between θ_{SH} of Nb and NbN is not possible but they are within the same order, suggesting that

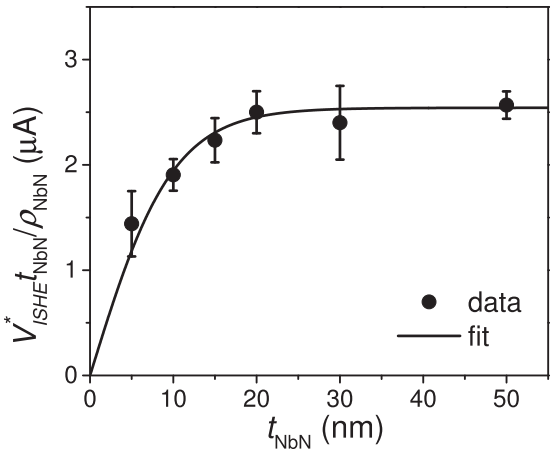

FIG. 7. $V_{\mathrm{ISHE}}t_{\mathrm{NbN}}/\rho_{\mathrm{NbN}}$ as a function of NbN thickness. We plot $V_{\mathrm{ISHE}}t_{\mathrm{NbN}}/\rho_{\mathrm{NbN}}$ to normalize V_{ISHE} with NbN thickness and resistivity. By using Eq. (3) in the main text, we extract the spin Hall angle (θ_{SH}) and spin-diffusion length (l_{SD}) of NbN to be 1.1×10^{-2} and 14 nm. The best-fit curve is shown along with the experimental data.

there are similar atomistic spin-orbit contributions from Nb atoms both for Nb and NbN. Details of this will be further clarified when more realistic theoretical studies of SHE in NbN become available.

As a final remark, we also performed FMR measurements as a function of temperature to determine the low-temperature spin pumping properties of NbN through the SC T_C. However, a significant increase of magnetic damping was observed as the temperature was lowered (this behavior is summarized in Appendix C). This enhanced damping complicated the investigation of V_{ISHE} across the SC T_C.

III. CONCLUSIONS

We determined the spin transport parameters of polycrystalline NbN thin films by the spin pumping technique using epitaxial YIG thin films at RT. We observe a modification of the YIG Gilbert damping parameter as a function of the variation of the NbN film thickness, confirming spin current injection in the NbN layer. By applying a spin-diffusion model, we have estimated $l_{\mathrm{SD}} = 14 \pm 3$ nm in NbN and $g_r^{\uparrow\downarrow} = 10 \pm 2\,\mathrm{nm}^{-2}$ at the NbN/YIG interface. From the NbN thickness dependence of the ISHE voltages, we determine θ_{SH} to be equal to -1.1×10^{-2}. We also compare l_{SD} of NbN extracted by three different techniques (thickness dependence of both α and V_{ISHE} as well as the Hanle measurements) and find good agreement between them. The measured parameters are a good reference to understand the NbN spin-orbit and spin transport properties and to aid the design of feasible spintronic experiments and devices in the normal and SC state.

ACKNOWLEDGMENTS

This work was supported by the Engineering and Physical Sciences Research Council through the Programme Grant "Superspin" (Grant No. EP/N017242/1), an International Network Grant (Grant No. EP/P026311/1), and studentship for A.S. (Grant No. EP/R512400/1).

APPENDIX A: DERIVATION OF FMR FIT CURVES

In normal dc FMR analysis, the measured dc voltage can be decomposed into symmetric and antisymmetric Lorentzian functions with respect to $\mu_0 H_{\mathrm{res}}$, with weights of A_{sym} and A_{asy}, respectively, leading to the following general power absorption expression [which is applicable both for FMR absorption (V_p) and ISHE voltage (V_{ISHE})]:

$$\begin{aligned} P_{\mathrm{dc}}(H) &= A_{\mathrm{sym}}(H) + A_{\mathrm{asy}}(H) + V_0 \\ &= A_{\mathrm{sym}} \frac{\Delta H^2}{(H - H_{\mathrm{res}})^2 + \Delta H^2} \\ &\quad + A_{\mathrm{asy}} \frac{\Delta H (H - H_{\mathrm{res}})}{(H - H_{\mathrm{res}})^2 + \Delta H^2} + V_0, \end{aligned} \tag{A1}$$

where V_0 is a background voltage. The first term gives the symmetric line shape and the second term produces the antisymmetric one. For FMR measurements based on ac magnetic field modulation, where an additional pair of coils on electromagnets provides small ac magnetic field, P_{ac} has the following relationship with P_{dc}:

$$P_{\mathrm{ac}} = \frac{dP_{\mathrm{dc}}}{dH} h_{\mathrm{ac}} \tag{A2}$$

where h_{ac} is the amplitude of ac magnetic field modulation. With these two equations, we can calculate P_{ac} as

$$\begin{aligned} P_{\mathrm{ac}}(H) &= -A_{\mathrm{sym}} h_{\mathrm{ac}} \frac{2(H - H_{\mathrm{res}})\Delta H^2}{\{(H - H_{\mathrm{res}})^2 + \Delta H^2\}^2} \\ &\quad - A_{\mathrm{asy}} h_{\mathrm{ac}} \frac{\Delta H\{(H - H_{\mathrm{res}})^2 + \Delta H^2\}}{\{(H - H_{\mathrm{res}})^2 + \Delta H^2\}^2}. \end{aligned} \tag{A3}$$

This equation was used to fit the ac field modulated signals, both V_{p} and V_{ISHE}, in our paper. The first term gives now the antisymmetric line shape and the second term produces the distorted symmetric one. Figures 8(a) and 8(b) display typical FMR data together with best fit curves using Eqs. (A1) and (A3), respectively, with corresponding extracted parameters presented in Fig. 8 as legends. We also checked that there was no experimental artifact by doing our ac experiments, by directly confirming that ac [Fig. 8(a)] and dc [Fig. 8(b)] measurements for the same experimental conditions generate the same fit parameters.

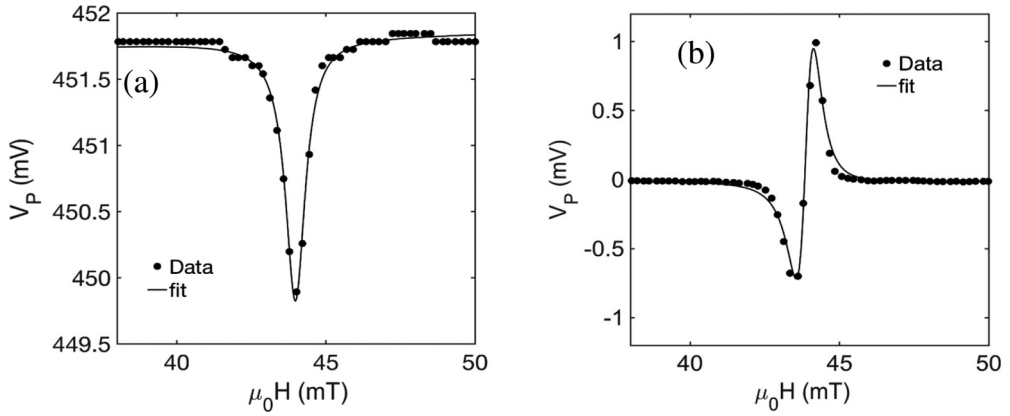

FIG. 8. Comparison of (a) ac and (b) dc V_{P} measurements. The extracted parameters using equations in Appendix A for each measurement method are depicted in the legends of the figures. We can confirm that the extracted values are almost the same for both measurements.

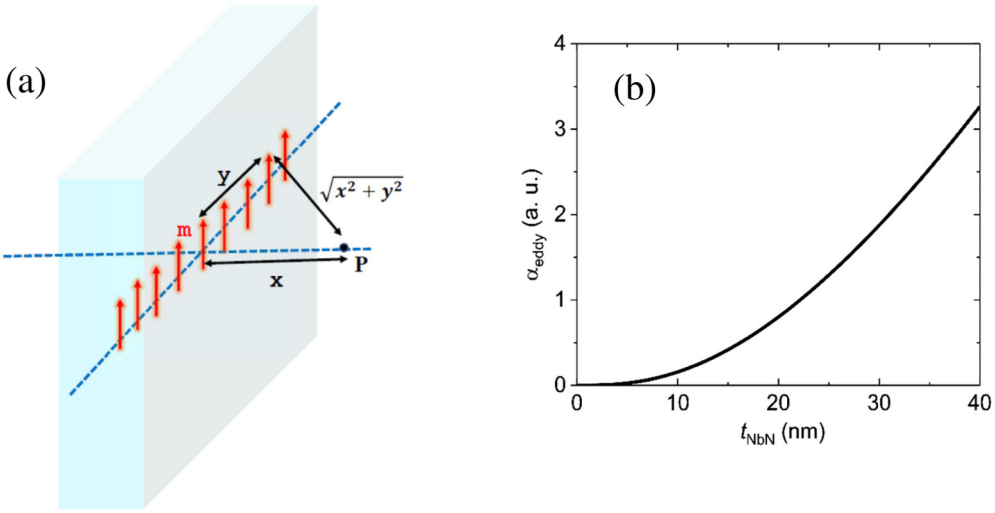

FIG. 9. Eddy current damping contribution. (a) A schematic of our model for the eddy current damping. A chain of magnetic moments (red arrow) lines up along the y direction and we consider the magnetic field at point P $(x, 0)$. (b) A plot of calculated eddy current damping as a function of the NbN thickness. The unit of the eddy current damping is arbitrary in order to discuss it qualitatively. The thickness dependence is clearly different from our experimental results in Fig. 3(b), suggesting that this damping mechanism is not significant in our experiments.

APPENDIX B: SIMPLIFIED MODEL FOR THE EDDY CURRENT DAMPING

We consider a slab of magnet containing a chain of distributed magnetic moments $\boldsymbol{m}$ as shown in Fig. 9(a). In order to model the eddy current damping in NbN, we first calculate the magnetic flux at point P where the distance between the point and the slab is x [Fig. 9(a)]. We can estimate the magnetic field at point P generated by a moment at $(0, y)$ using the Biot-Savart law, as

$$B = \frac{\mu_0}{4\pi}\frac{m}{(x^2+y^2)^{3/2}} \tag{B1}$$

where μ_0 is the permeability of free space. We assume that the length of the chain is infinitely long, which is a valid assumption by taking into consideration that the film thickness is much shorter than the sample lateral dimensions. By integrating the contribution of the individual moments, we calculate the total magnetic field B_{total} as

$$B_{\text{total}} = 2\int_0^\infty \frac{\mu_0}{4\pi}\frac{m}{(x^2+y^2)^{3/2}}dy = \frac{\mu_0}{2\pi}\frac{m}{x^2}. \tag{B2}$$

Using this B_{total} expression within this quasi-two-dimensional picture, we can calculate the magnetic flux Φ at point P. By definition, $\Phi = \iint B_{\text{total}} ds$, where the integration surface is defined by the thickness t_{NbN} and the width w of the NbN film. This reads

$$\begin{aligned}\Phi &= \iint B_{\text{total}} ds = w \times \int_{t_{\text{YIG}}/2}^{\frac{t_{\text{YIG}}}{2}+t_{\text{NbN}}} \frac{\mu_0}{2\pi}\frac{m}{x^2}dx \\ &= \frac{\mu_0 wm}{\pi}\frac{t_{\text{NbN}}}{t_{\text{YIG}}(t_{\text{YIG}}+2t_{\text{NbN}})}.\end{aligned} \tag{B3}$$

For the definition of the integration region, we assume that the chain of the magnetic moments is located at the center of the YIG film.

After estimating the magnetic flux, we can calculate the radiative dissipation power P as

$$P = \frac{\omega}{2Z_{\text{NbN}}}\Phi^2 = \frac{\omega}{2Z_{\text{NbN}}}\left(\frac{\mu_0 wm}{\pi}\frac{t_{\text{NbN}}}{t_{\text{YIG}}(t_{\text{YIG}}+2t_{\text{NbN}})}\right)^2. \tag{B4}$$

Here Z_{NbN} is the impedance of the NbN film and for simplification we assume that the real part (resistance) dominates, meaning that $Z_{\text{NbN}} \approx R_{\text{NbN}} = \rho_{\text{NbN}}(d/wt_{\text{NbN}})$. Using the total nonequilibrium magnon energy generated during the experiments as $\hbar\omega NV$ (here, N is the number of the nonequilibrium magnons and V is the volume of YIG), we can express the rate of energy dissipation as

$$\frac{1}{\tau} = \frac{P}{E} = \frac{\omega\, wt_{\text{NbN}}}{2\rho_{\text{NbN}}d\hbar\omega N}\left(\frac{\mu_0 wm}{\pi}\frac{t_{\text{NbN}}}{t_{\text{YIG}}(t_{\text{YIG}}+2t_{\text{NbN}})}\right)^2. \tag{B5}$$

Finally, the damping component caused by eddy currents generated by the time-dependent flux change can be given by

$$\begin{aligned}\alpha_{\text{eddy}} &= \frac{1}{2\omega}(1/\tau) \\ &= \frac{wt_{\text{NbN}}}{4\rho_{\text{NbN}}d\hbar\omega NV}\left(\frac{\mu_0 wm}{\pi}\frac{t_{\text{NbN}}}{t_{\text{YIG}}(t_{\text{YIG}}+2t_{\text{NbN}})}\right)^2.\end{aligned} \tag{B6}$$

As this model is a simplified one, we only discuss α_{eddy} qualitatively. In particular, we can extract the NbN thickness dependence of α_{eddy} by using this expression and find that it is proportional to $(\frac{t_{\text{NbN}}{}^{3/2}}{t_{\text{YIG}}+2t_{\text{NbN}}})^2$. We plot the dependence in Fig. 9(b), which indicates that the damping based on this mechanism should monotonically increase with thickness. However, this trend is different from what we experimentally observed, where α becomes constant for the larger thickness limit. This suggests that the damping mechanism through the eddy current in the NbN layers is not significant and can

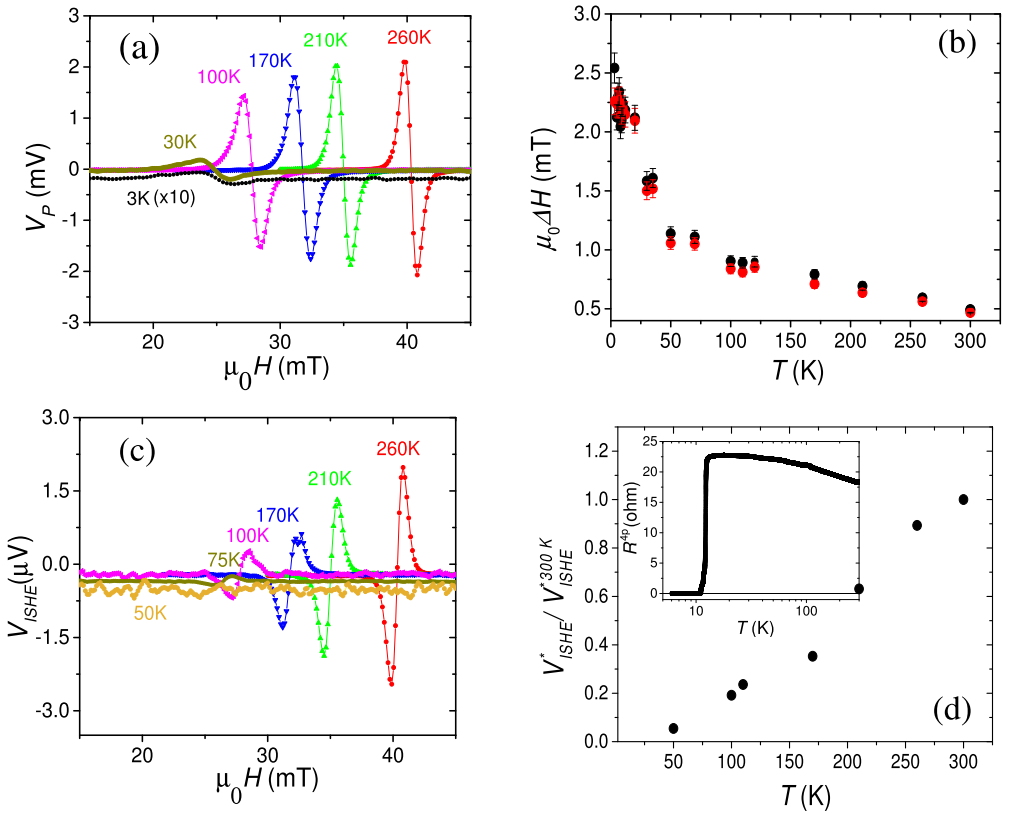

FIG. 10. FMR absorption spectra and ISHE voltages as a function of temperature for the $t_{NbN} = 10$ nm sample. (a) FMR absorption spectra measured at 3 GHz, with temperature ranging from 260 to 3 K. (b) Linewidth evolution with temperature for the 3-GHz measurements. Black data correspond to a YIG/NbN sample and red data correspond to a bare YIG sample. (c) ISHE voltages measured at 3 GHz for the temperature region of 50–300 K. We confirm that the peak height is below the signal-to-noise ratio around 50 K. (d) The normalized ISHE voltage amplitude as a function of temperature. The inset represents our four point probe measurements of NbN resistivity (for $t_{NbN} = 10$ nm).

be neglected for the examined NbN thicknesses. Moreover, the work by Flovik *et al.* [45] discusses the eddy current effect on the line shape of the FMR spectrum. Flovik *et al.* showed that when eddy currents exist in an FM/NM bilayer the FMR line shape can be significantly affected, varying from a pure symmetric shape to a mixture of symmetric and antisymmetric ones. Experimentally, we have not observed a strong A_{asy} component, suggesting that the eddy current in our NbN film does not play a significant role in our measurements. In addition, similar eddy current and radiative damping mechanisms have also been discussed by Schoen *et al.* [46]. They demonstrated that when their sample is placed 100 μm away from the waveguide radiative damping with the waveguide is largely suppressed. Since we also inserted an insulating tape between our samples and the waveguide, we believe that the radiative damping is minor in our experiments. Furthermore, Qaid *et al.* [47] reported that although eddy current damping can be observed in a weak spin-orbit material (in their case a conducting polymer) this is not the case for a high spin-orbit metal (Pt). For instance, they showed that the damping enhancement in a YIG/Pt structure can still be dominated by the spin pumping effect in Pt. Since our NbN is a sufficiently high spin-orbit material, we believe that the eddy current component is much smaller (an order of magnitude at least) than that of spin pumping into NbN.

APPENDIX C: LOW-TEMPERATURE MEASUREMENTS OF SPIN PUMPING IN NbN/YIG SAMPLES

It is widely reported that YIG thin films tend to show significant temperature-dependent magnetic damping [32,33,48,49], where the superb damping character at RT is lost when the films are cooled to lower temperatures. The origin of this remains under debate but enhanced low-temperature two-magnon scattering (due to interfacial defects in ultrathin films) [32] in combination with rare-earth or Fe^{2+} impurity scattering [50,51] are likely mechanisms. Jermain *et al.* [33] discuss that, if the FMR linewidth has a peaked temperature dependence that dominates over the proportionality expected with $M_S(T)$ increase, impurity scattering is the more likely mechanism. Although the nature of the impurities remains ambiguous, other reports of the high-frequency characterization of PLD-grown and sputtered YIG thin films have pointed out the likely significance of Gd^{3+} diffusion from the GGG substrate [52–54].

Our own extensive FMR measurements of bare YIG on GGG (of comparable thicknesses) [55] show that, when Gd^{3+} impurities are concentrated in a thin (1–5 nm) layer near the substrate interface, they form a ferromagnetic sublattice that, as its moment increases at low temperatures, opposes the net YIG magnetization [50,56], and also introduces magnetic

disorder and additional damping channels that dominate the film's FMR response.

Here we describe the low-temperature characterizations of our YIG/NbN samples. Figure 10 summarizes both FMR absorption spectra and ISHE voltages as a function of temperature for the sample with NbN thickness of 10 nm. With decreasing temperature, there is a clear increase of ΔH, leading to a corresponding reduction of the FMR absorption signal, as shown in Fig. 10(a). The FMR spectrum at 3 K can be extracted by taking multiple scans to improve the signal-to-noise ratio through data averaging. Figure 10(b) shows that ΔH increases by a factor of 5 between 300 and 3 K, with a steep enhancement below 100 K. For direct comparison we present data in Fig. 10(b) both of YIG/NbN (black points) and bare YIG samples (red points). It is clear that linewidth enhancement at low temperatures is due to YIG. In comparison with the previous low-temperature FMR studies on YIG, we can detect an FMR signal down to 3 K in the MW transmission geometry, possibly owing to a relatively thick film. Unfortunately, the ΔH enhancement significantly hindered our ISHE detection plotted in Figs. 10(c) and 10(d). The voltage peak is comparable to or below the noise level at 50 K and it was not possible to investigate the evolution of V_{ISHE} across the T_C of NbN, which is 11 K for the 10-nm film, measured by the four point dc resistance R^{4p} shown in the inset of Fig. 10(d). To study the spin transport properties in NbN across T_C, by spin pumping technique, would require an improvement of YIG thin-film quality to overcome the observed ΔH enhancement. We note that a very recent work by Umeda *et al.* exploited the spin-Seebeck effect as a spin-injection method, demonstrating an interesting coherent peak in spin-Seebeck coefficient related to the quasiparticle spin transport [29].

[1] J. Sinova, S. O. Valenzuela, J. Wunderlich, C. H. Back, and T. Jungwirth, Rev. Mod. Phys. **87**, 1213 (2015).

[2] J. Bass and W. P. Pratt, Jr., J. Phys.: Condens. Matter **19**, 183201 (2007).

[3] Y. Tserkovnyak, A. Brataas, and G. E. W. Bauer, Phys. Rev. Lett. **88**, 117601 (2002).

[4] S. O. Valenzuela and M. Tinkham, Nature (London) **442**, 176 (2006).

[5] T. Kimura, Y. Otani, T. Sato, S. Takahashi, and S. Maekawa, Phys. Rev. Lett. **98**, 156601 (2007).

[6] M. Morota, Y. Niimi, K. Ohnishi, D. H. Wei, T. Tanaka, H. Kontani, T. Kimura, and Y. Otani, Phys. Rev. B **83**, 174405 (2011).

[7] G. Mihajlovic, J. E. Pearson, M. A. Garcia, S. D. Bader, and A. Hoffmann, Phys. Rev. Lett. **103**, 166601 (2009).

[8] S. Mizukami, Y. Ando, and T. Miyazaki, Phys. Rev. B **66**, 104413 (2002).

[9] E. Saitoh, M. Ueda, H. Miyajima, and G. Tatara, Appl. Phys. Lett. **88**, 182509 (2006).

[10] O. Mosendz, J. E. Pearson, F. Y. Fradin, G. E. W. Bauer, S. D. Bader, and A. Hoffmann, Phys. Rev. Lett. **104**, 046601 (2010).

[11] K. Ando, S. Takahashi, J. Ieda, H. Kurebayashi, T. Trypiniotis, C. H. W. Barnes, S. Maekawa, and E. Saitoh, Nat. Mater. **10**, 655 (2011).

[12] E. Shikoh, K. Ando, K. Kubo, E. Saitoh, T. Shinjo, and M. Shiraishi, Phys. Rev. Lett. **110**, 127201 (2013).

[13] S. Watanabe, K. Ando, K. Kang, S. Mooser, Y. Vaynzof, H. Kurebayashi, E. Saitoh, and H. Sirringhaus, Nat. Phys. **10**, 308 (2014).

[14] D. Sun, K. J. van Schooten, M. Kavand, H. Malissa, C. Zhang, M. Groesbeck, C. Boehme and Z. V. Vardeny, Nat. Mater. **15**, 863 (2016).

[15] Z. Tang, E. Shikoh, H. Ago, K. Kawahara, Y. Ando, T. Shinjo, and M. Shiraishi, Phys. Rev. B **87**, 140401(R) (2013).

[16] Y. Shiomi, K. Nomura, Y. Kajiwara, K. Eto, M. Novak, K. Segawa, Y. Ando, and E. Saitoh, Phys. Rev. Lett. **113**, 196601 (2014).

[17] M. Harder, Y. Gui, and C.-M. Hu, Phys. Rep. **661**, 1 (2016).

[18] A. Tsukahara, Y. Ando, Y. Kitamura, H. Emoto, E. Shikoh, M. P. Delmo, T. Shinjo, and M. Shiraishi, Phys. Rev. B **89**, 235317 (2014).

[19] L. Chen, S. Ikeda, F. Matsukura, and H. Ohno, Appl. Phys. Express **7**, 013002 (2014).

[20] Y. Kajiwara *et al.*, Nature (London) **464**, 262 (2010).

[21] J. Linder and J. W. A. Robinson, Nat. Phys. **11**, 307 (2015).

[22] J. Y. Juang and D. A. Rudman, *Advances in Cryogenic Engineering Materials*, edited by R. P. Reed and A. F. Clark (Plenum, New York, 1986), Vol. 32, p. 651.

[23] A. Pal, Z. H. Barber, J. W. A. Robinson, and M. G. Blamire, Nat. Commun. **5**, 3340 (2014).

[24] K. Senapati, M. G. Blamire, and Z. H. Barber, Nat. Mater. **10**, 849 (2011).

[25] A. Pal, K. Senapati, Z. H. Barber, and M. G. Blamire, Adv. Mater. **25**, 5581 (2013).

[26] A. Pal, J. A. Ouassou, M. Eschrig, J. Linder, and M. G. Blamire, Sci. Rep. **7**, 40604 (2017).

[27] T. Wakamura, H. Akaike, Y. Omori, Y. Niimi, S. Takahashi, A. Fujimaki, S. Maekawa, and Y. Otani, Nat. Mater. **14**, 675 (2015).

[28] Y. Yao, Q. Song, Y. Takamura, J. P. Cascales, W. Yuan, Y. Ma, Y. Yun, X. C. Xie, J. S. Moodera, and W. Han, Phys. Rev. B **97**, 224414 (2018).

[29] M. Umeda, Y. Shiomi, T. Kikkawa, T. Niizeki, J. Lustikova, S. Takahashi, and E. Saitoh, Appl. Phys. Lett. **112**, 232601 (2018).

[30] M. Eschrig, Rep. Prog. Phys. **78**, 104501 (2015).

[31] E. E. Anderson, Phys. Rev. **134**, A1581 (1964).

[32] N. S. Sokolov *et al.*, J. Appl. Phys. **119**, 023903 (2016).

[33] C. L. Jermain, S. V. Aradhya, N. D. Reynolds, R. A. Buhrman, J. T. Brangham, M. R. Page, P. C. Hammel, F. Y. Yang, and D. C. Ralph, Phys. Rev. B **95**, 174411 (2017).

[34] O. d'Allivy Kelly *et al.*, App. Phys Lett. **103**, 082408 (2013).

[35] H. L. Wang, C. H. Du, Y. Pu, R. Adur, P. C. Hammel, and F. Y. Yang, Phys. Rev. Lett. **112**, 197201 (2014).

[36] Y. Tserkovnyak, A. Brataas, G. E. W. Bauer, and B. I. Halperin, Rev. Mod. Phys. **77**, 1375 (2005).

[37] K. Ando *et al.*, J. Appl. Phys. **109**, 103913 (2011).

[38] K. Ando and E. Saitoh, Nat. Comms. **3**, 629 (2012).

[39] K. R. Jeon, C. Ciccarelli, H. Kurebayashi, J. Wunderlich, L. F. Cohen, S. Komori, J. W. A. Robinson, and M. G. Blamire, Phys. Rev. Appl. **10**, 014029 (2018).

[40] L. Zhang *et al.*, Scientific Reports **8**, 1486 (2018).

[41] L. Q. Liu, R. A. Buhrman, and D. C. Ralph, arXiv:1111.3702.

[42] A. R. Melnik *et al.*, Nature (London) **511**, 449 (2014).
[43] Y. Fan *et al.*, Nat. Mater. **13**, 699 (2014).
[44] P. Deorani *et al.*, Phys. Rev. B **90**, 094403 (2014).
[45] V. Flovik, F. Macia, A. D. Kent, and E. Wahlstrom, J. Appl. Phys. **117**, 143902 (2015).
[46] M. A. W. Schoen, J. M. Shaw, H. T. Nembach, M. Weiler, and T. J. Silva, Phys. Rev. B **92**, 184417 (2015).
[47] M. M. Qaid, T. Richter, A. Müller, C. Hauser, C. Ballani, and G. Schmidt, Phys. Rev. B **96**, 184405 (2017).
[48] E. Shigematsu, Y. Ando, R. Ohshima, S. Dushenko, Y. Higuchi, T. Shinjo, H. J. von Bardeleben, and M. Shiraishi, Appl. Phys. Express **9**, 053002 (2016).
[49] R. Ohshima, H. Emoto, T. Shinjo, Y. Ando, and M. Shiraishi, J. Appl. Phys. **117**, 17D136 (2015).
[50] M. Sparks, *Ferromagnetic-Relaxation Theory* (McGraw-Hill, New York, 1964).
[51] G. F. Dionne, *Magnetic Oxides* (Springer, New York, 2010).
[52] E. L. Jakubisova, S. Visnovsky, H. Chang, and M. Wu, Appl. Phys. Lett. **108**, 082403 (2016).
[53] A. Mitra, O. Cespedes, Q. Ramasse, M. Ali, S. Marmion, M. Ward, R. M. D. Brydson, C. J. Kinane, J. F. K. Cooper, S. Langridge, and B. J. Hickey, Sci. Rep. **7**, 11774 (2017).
[54] J. M. Gomez-Perez *et al.*, Phys. Rev. Appl. **10**, 044046 (2018).
[55] L. McKenzie-Sell, M. Amado, G. Kimbell, G. Divitini, C. Ciccarelli, and J. W. A. Robinson (unpublished).
[56] T. Yamagishi, J. Awaka, Y. Kawashima, M. Uemura, S. Ebisu, S. Chikazawa, and S. Nagata, Philos. Mag. **85**, 1819 (2005).